Study of terbium production from enriched Gd targets via the reaction ^{155}Gd(d,2n)^{155}Tb

Yizheng Wang, Thomas Sounalet, Arnaud Guertin, Etienne Nigron, Nathalie Michel, Ferid Haddad

To cite this version:

Yizheng Wang, Thomas Sounalet, Arnaud Guertin, Etienne Nigron, Nathalie Michel, et al.. Study of terbium production from enriched Gd targets via the reaction ^{155}Gd(d,2n)^{155}Tb. Applied Radiation and Isotopes, 2023, 201, pp.110996. 10.1016/j.apradiso.2023.110996 . hal-04197419

HAL Id: hal-04197419

https://hal.science/hal-04197419v1

Submitted on 23 Oct 2023

Study of terbium production from enriched Gd targets via the reaction 155Gd(d,2n)155Tb

Yizheng Wang [a], Thomas Sounalet [a], Arnaud Guertin [a], Etienne Nigron [b], Nathalie Michel [a,b], Férid Haddad [a,b]

[a] Subatech, UMR 6457, IMT Atlantique, CNRS/IN2P3, Nantes Université, 4 rue Alfred Kastler BP20722, 44307 Nantes Cedex 3 France

[b] ARRONAX Cyclotron, 1 rue Aronnax, CS10112, 44817 Saint-Herblain Cedex, France

(*corresponding writer, email address:wangy@subatech.in2p3.fr
Present address: 4 rue Alfred Kastler, 44307 Nantes, France)

Abstract

The terbium (Tb) family has attracted much attention in recent years thanks to the diagnostic and therapeutic applications of the quadruplet ^{149}Tb, ^{152}Tb, ^{155}Tb and ^{161}Tb. However, the shortage of Tb supply is one of the main reasons hindering its clinical applications. To increase its availability, this work proposes to use enriched gadolinium (Gd) targets to produce some Tb isotopes (^{149}Tb, ^{152}Tb, and ^{155}Tb) via proton-or-deuteron-induced reactions in cyclotrons, the involved reactions are ^{152}Gd(p,4n)^{149}Tb, ^{152}Gd(p,n)^{152}Tb, ^{155}Gd(p,n)^{155}Tb and ^{155}Gd(d,2n)^{155}Tb. The production of the Auger and gamma emitter ^{155}Tb is first taken as a case study because the enrichment level of ^{155}Gd target is higher (92.8%) compared to other stable Gd isotopes. Using enriched thin Gd-containing targets, cross-sections of the reaction ^{155}Gd(d,x)^{153,154,155,156}Tb have been measured at the GIP ARRONAX cyclotron facility with a beam energy ranging from 8 MeV to 30 MeV. This measurement is helpful to estimate the production yield and the purity of ^{155}Tb, and also to determine the irradiation parameters for large production batches. A thick enriched $^{155}Gd_2O_3$ target has been then irradiated with an incident energy of 15.1 MeV and a beam intensity of 368 nA for 1 h. The production yield of ^{155}Tb is 10.2 MBq/µAh at End Of Bombardment (EOB) and the purity is 89% after 14 days of decay. These experimental values are consistent with estimations. A comparison of the deuteron-induced and proton-induced production routes is also presented in this paper.

Keywords: terbium production, enriched gadolinium target, cross-section measurement, deuteron irradiation, theranostics radioisotope, cyclotron-produced radionuclide

1. Introduction

Theranostics, a combination of a diagnostic test and a therapeutic process, was first proposed in the 1990s (Herzog et al., 1993) and developed rapidly in the last decade. In nuclear medicine, the core idea behind the theranostics is to use a pair of radionuclides with similar chemical properties to achieve the diagnostic and the therapy (Yordanova et al., 2017). The first proposed theranostics radionuclide pair is the ^{86}Y/^{90}Y pair for the treatment of breast cancer (Herzog et al., 1993). Since then, several radionuclide combinations have been investigated or suggested, such as ^{68}Ga/^{177}Lu, ^{44g}Sc/^{47}Sc, ^{64}Cu/^{67}Cu, ^{83}Sr/^{89}Sr and ^{124}I/^{131}I (Qaim et al., 2018). The interest in terbium radionuclides has grown considerably, with multiple potential applications identified for specific isotopes. For example, ^{149}Tb has shown promise as a candidate for targeted alpha therapy (Beyer et al., 2004), while ^{152}Tb could be used in Positron Emission Tomography (PET) imaging (Müller et al., 2012). Additionally, ^{155}Tb has potential applications in the Singlephoton Emission Computed Tomography (SPECT) imaging (Müller et al., 2014) and Auger therapy (Duchemin et al., 2016), and the ^{161}Tb is being considered as a complement to ^{177}Lu for β-therapy (Müller et al., 2012, Baum et al., 2021). This is why terbium is called the "Swiss knife" of nuclear medicine. However, applications of Tb radionuclides are limited nowadays because of their low availability.

Several production routes, using nuclear reactors or accelerators, have been developed to produce Tb radionuclides. For example, nuclear reactors are used to produce ^{161}Tb through the reaction ^{160}Gd(n, γ)^{161}Gd → ^{161}Tb. Despite an indirect production route, the production yield of ^{161}Tb is large: with 33 mg of highly enriched $^{160}Gd_2O_3$ target, the production of ^{161}Tb can reach up to 20 GBq (Gracheva et al., 2019). Meanwhile, other Tb radionuclides, such as ^{149}Tb, ^{152}Tb, and ^{155}Tb, are mostly produced by spallation reactions on natural tantalum targets through the reaction ^{nat}Ta(p,x)^{149,152,155}Tb. This production route has several limitations: on one hand, there are few high-energy accelerator facilities; on the other hand, this route needs an expensive online mass separation procedure to isolate the desired radionuclide with, today, a low efficiency (Duchemin et al., 2020). Heavy-ion-induced reactions have also been considered to produce ^{149}Tb and ^{152}Tb (Lahiri et al., 1999; Nayak et al., 1999; Allen et al., 2001; Maiti, 2011). However, most of these studies were from two decades ago, the authors did not study impurities and purification issues, and the yield of ^{152}Tb was relatively small. Furthermore, the limited number of heavy ion accelerator facilities is also a disadvantage of this production route. As an alternative, the use of light-charged particles has been studied in recent years to produce Tb radionuclides. Natural Gd target was first considered (Vermeulen et al., 2012; Tárkányi et al., 2013; Szelecsényi et al., 2016; Duchemin et al., 2016; Formento-Cavaier et al., 2020), but it shows poor yield and low purity. Therefore, enriched gadolinium targets may overcome these two issues, the involved reactions are ^{152}Gd(p,4n)^{149}Tb (Steyn et al., 2014), ^{152}Gd(p,n)^{152}Tb (Güray et al., 2015), ^{155}Gd(p,4n)^{152}Tb (Steyn et al., 2014), and ^{155}Gd(p,n)^{155}Tb (Dellepiane et al., 2022). Besides this, light-charged particles induced reactions require relatively low energies (5-70 MeV), especially for ^{152}Tb and ^{155}Tb (5-12 MeV), starting from enriched ^{152}Gd and ^{155}Gd respectively, that are reachable for many biomedical cyclotrons. Therefore, this production route has the potential to increase Tb supply given the large number of accelerator centers that continue to expand each year.

The above reactions use only protons. Despite cross-sections of deuteron-induced reactions are often greater than those of proton ones, leading to more productive production routes, research on deuteron-induced reactions is rare. Hence, the objective of this study is to explore the deuteron production route on enriched gadolinium to produce terbium radionuclides. For this, the production of ^{155}Tb is taken as a case study. In this case, targets contain enriched ^{155}Gd and the nuclear reaction of interest is ^{155}Gd(d,2n)^{155}Tb. There are three main steps in this work: first measuring the production cross-section of this reaction and all parasitic ones especially those leading to Tb isotopes, second estimating the production yield and purity of ^{155}Tb based on the obtained cross-section values and finally performing a thick target irradiation to validate our calculated yields and prepare for large batch production. Thin enriched Gd-containing targets were used for cross-section measurements while a thick enriched $^{155}Gd_2O_3$ pellet was used for thick target irradiation.

2. Materials and methods

Target preparation

The enriched $^{155}Gd_2O_3$ powder, provided by TraceScience, has an enrichment level of 92.8%. The isotopic composition of the enriched Gd is shown in Table 1. The proportion of ^{156}Gd is still quite large (5.7%) while the proportion of other isotopes ^{157,158,160}Gd is less than 1%. This powder is noted as $^{*}Gd_2O_3$ in this work.

Table 1 Isotopic composition of the enriched $^{*}Gd_2O_3$.

Isotope	^{155}Gd	^{156}Gd	^{157}Gd	^{158}Gd	^{160}Gd
Proportion (%)	92.8	5.7	0.8	0.5	0.2

Using this enriched powder, thin targets were first prepared for cross-section measurements through the co-electrodeposition technique where Gd_2O_3 and nickel are used. In this technique, Ni from alkaline Ni^{2+} electrolyte is deposited and at the same time, $^{*}Gd_2O_3$ particles mixed in the electroplating solution are transported mechanically into the Ni deposit. The obtained target is a Ni-$^{*}Gd_2O_3$ composite deposit. The substrate is a 50-µm-thick gold foil provided by Goodfellow (99.95% purity). Details of experimental parameters and the proof-of-concept were presented in a previous work (Wang et al., 2022). Using this technique, 10 targets were prepared for this work, noted as target #1 to #10. For each target, the diameter was about 1.5 cm, the thickness varied between 8 µm and 18 µm along with the duration of the deposition process (from 35 to 60 min) leading to a Gd content between 0.7 mg and 2.0 mg. This Gd content was measured by the *Thermo Scientific iCAP 6000 Series* Inductively Coupled Plasma - Atomic Emission Spectrometry (ICP-AES) after the dissolution of the targets in 10 mL of 12 M HCl. The photo of one thin target (target #4) is shown in Fig. 1.

Fig. 1 The photo of a thin target (target #4) made by co-electrodeposition technique. The thickness is 18 µm and the diameter of the deposit is 1.5 cm.

For thick target irradiation, an enriched $^{*}Gd_2O_3$ target was prepared by the pelletizing method. The principle is to convert fine powder into a pellet by compressing and molding. Using 0.63 g of enriched $^{*}Gd_2O_3$ powder, a pellet with a diameter of 20 mm and a thickness of 390 µm was made under 600 bar (Fig. 2 (a)). The pellet was first wrapped by hand in two 10-µm-thick aluminum (Al) foils (Fig. 2 (b)) provided by Goodfellow (99.1% purity). Then the assembly was pressed for 60 s under 600 bar (Fig. 2 (c)) to finally get a tightly wrapped pellet (Fig. 2 (d)).

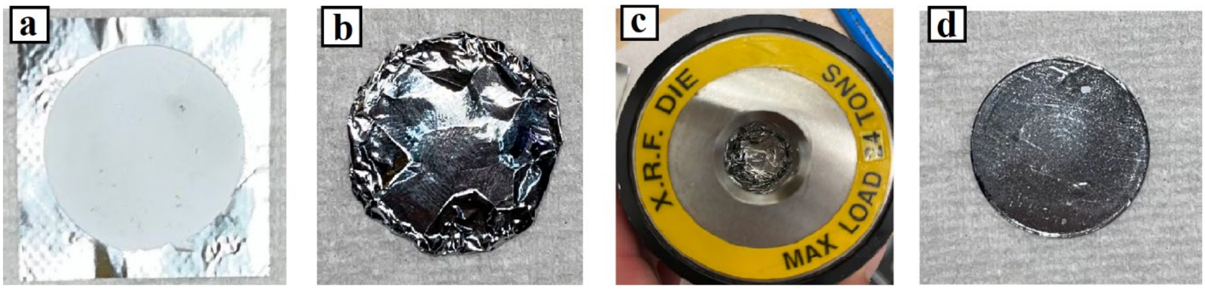

Fig. 2 Packaging process of the thick $^{*}Gd_2O_3$ pellet: (a) the enriched pellet made by the press; (b) the hand wrapped pellet by two aluminum foils; (c) the wrapped pellet in the press die; (d) the tightly wrapped pellet after the compression.

Preparation for cross-section measurements

The stacked foils technique was used to measure cross-sections. Each stack was composed of two targets, two groups of titanium (Ti) and nickel (Ni) monitor foils, and an Al degrader foil. All foils were supplied by Goodfellow, the purity is above 99.95% for Ti and Ni, and 99.1% for Al. The stack was encapsulated and sealed in a stainless steel metal ring capsule with a 20-µm-diameter hole in the center. The assembly was placed in air 6 cm downstream of the beam output window (a 50 µm thick Kapton foil). The schematic diagram of a stack and a photo of target and the capsule are presented in Fig. 3.

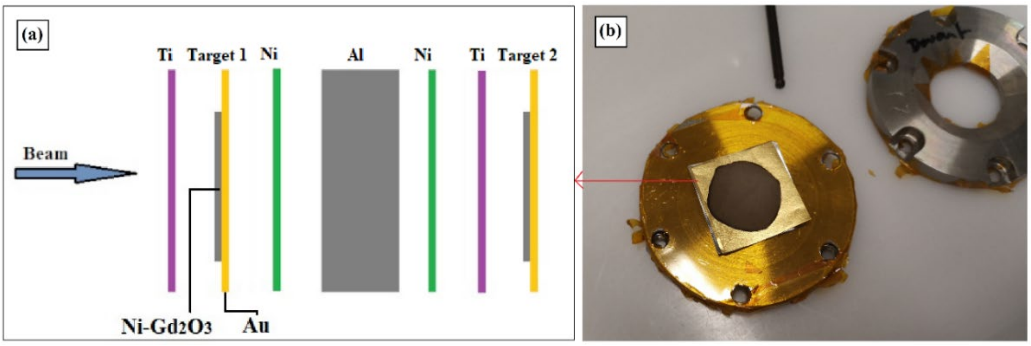

Fig. 3 (a) Schematic diagram of the stack composition used for a typical experiment where two targets were irradiated simultaneously. The size and thickness of the foils are not drawn according to the real scale. (b) Photo of the stack (without the first Ti foil) and the two parts of the capsule.

The irradiation process was carried out at GIP ARRONAX cyclotron facility. Ten thin targets were irradiated by pair in 5 experiments (see details in Table 2), referenced as experiment A, B, C, D and E, over a period of few months. The Gd content was measured by ICP-AES after irradiation. The incident energy hitting the target was estimated by TRIM (Ziegler et al., 2010), the energy at the middle thickness was taken to represent the incident energy in the target. As shown in Table 2, neighbor data points were measured in different irradiation experiments in order to prevent any systematic error coming from one experiment. For each experiment, the beam intensity was about 50 nA and the irradiation time was 30 min.

The cross-section determination remains the same as the one used in our previous work (Wang et al., 2022) and is based on *eq.1*:

$$\sigma\,(E) = \frac{Act(E) \cdot A}{\chi \cdot I \cdot N_A . \rho \cdot \delta x \cdot (1 - e^{-\lambda t})} \qquad (eq.1)$$

where *Act (E)* (Bq) is the activity of Tb radionuclides produced at energy *E*, *A* (g.mol^{-1}) is the molar mass of the target nuclei, χ (%) is the purity of the target, *I* (s^{-1}) is the number of projectile per second hitting the target, N_A (atom·mol^{-1}) is the Avogadro number, ρ (g.cm^{-3}) is the target material bulk density, δx (cm) is the thickness of the target, λ (s^{-1}) is the decay constant of Tb radionuclides, and *t* (s) is the irradiation time.

The activity *Act (E)* was measured by a *CANBERRA* high-purity germanium detector (HPGe). Two reference sources, with the same geometry as the samples, were used for energy and efficiency calibrations: one ^{152}Eu source for calibrating solid samples (monitor foils) and one multi-gamma source (^{210}Pb, ^{241}Am, ^{109}Gd, etc) provided by GIP ARRONAX for calibrating liquid samples (targets). The dissolved target sample was placed in contact with the detector head. The data acquisition began 20 h after the end of bombardment (EOB) for the first target and 38 h after the EOB for the second target. The counting duration was between 8 h to 14 h for each sample. The dead time was between 1% to 5%. The investigated Tb radionuclides are ^{153}Tb, ^{154g}Tb, ^{154m1}Tb, ^{154m2}Tb, ^{155}Tb, and ^{156}Tb, their decay information and reaction information are listed in Table 3. The E_γ and I_γ listed in the table are gamma energy and associated emission intensity that we used to determine the radionuclide's activity.

Table 2 Target information of the irradiation for enriched targets.

Experiment	Target number	Gd content (mg)	Energy (MeV)
A	1	1.5	8.1 ± 0.4
B	2	1.0	10.4 ± 0.4
C	3	1.6	11.2 ± 0.4
B	4	1.5	12.4 ± 0.3
D	5	1.2	14.0 ± 0.4
A	6	1.5	14.2 ± 0.3
C	7	2.0	16.0 ± 0.3
D	8	1.4	19.4 ± 0.3
E	9	0.7	24.4 ± 0.4
E	10	0.7	29.7 ± 0.3

Table 3 Decay information and relative reactions of terbium radionuclides, ^{48}V and ^{58}Co ("Decay data search," n.d.; "NuDat 3," n.d.). The $E_{threshold}$ represents the threshold energy of the reaction to produce the ground state radionuclide.

Radionuclide	Half-life $T_{1/2}$	E_γ (keV)	I_γ (%)	Nuclear Reaction	$E_{threshold}$ (MeV)
^{153}Tb	2.34 d	212.00	28.5	^{155}Gd (d,4n) ^{156}Gd (d,5n)	20.17 28.81
^{154g}Tb	21.5 h	1291.326	6.9	^{155}Gd (d,3n)	13.16
^{154m1}Tb	9.4 h	540.18	20	^{156}Gd (d,4n)	21.81
^{154m2}Tb	22.7 h	426.78	17	^{157}Gd (d,5n)	28.25

^{155}Tb	5.32 d	180.08	7.5	^{155}Gd (d,2n)	3.88
				^{156}Gd (d,3n)	12.52
				^{157}Gd (d,4n)	18.96
				^{158}Gd (d,5n)	27.00
				^{160}Gd (d,7n)	40.56
^{156g}Tb	5.35 d	534.29	67	^{155}Gd (d,n)	0.00
		1222.44	31	^{156}Gd (d,2n)	5.52
^{156m1}Tb	24.4 h	49.630	74.1	^{157}Gd (d,3n)	11.96
^{156m2}Tb	5.3 h	88.4	1.15	^{158}Gd (d,4n)	20.00
				^{160}Gd (d,6n)	33.56
^{48}V	15.97 d	983.525	99.98	^{nat}Ti(d,x)^{48}V	0.00
		1312.105	98.2		
^{58}Co	70.86 d	810.7593	99.450	^{nat}Ni(d,x)^{58}Co	0.00

The number of projectile per second hitting the target I is determined using monitor foils through the reference reactions ^{nat}Ti(d,x)^{48}V and ^{nat}Ni(d,x)^{58}Co. The decay information for ^{48}V and ^{58}Co are also listed in Table 3. Titanium monitor foils were measured by the same detector 19 days after EOB to allow the full decay of ^{48}Sc ($T_{1/2}$ = 43.67 h, E = 983.526 keV, I_γ = 100.1%) and avoid interferences (Nigron et al., 2021). Similarly, nickel monitor foils were measured 2 months after EOB to avoid interferences of ^{56}Ni ($T_{1/2}$ = 6.075 d, E = 811.85 keV, I_γ = 86.0%) (Hermanne et al., 2013). All monitor foils were counted from 8 h to 14 h at 19 cm from the detector. The dead time is close to 0%.

Methods for production yield and purity estimation

Using the measured cross-sections, the production yield and the radionuclide purity were estimated and later used to determine irradiation parameters and to optimize thick target production.

The production yield represents the efficiency of the production during an irradiation process, it can be estimated as *eq.2*:

$$Y(t) = \frac{\chi \cdot N_A \cdot \lambda}{Z \cdot e \cdot A} \int_{E_1}^{E_0} \frac{\sigma(E)}{dE/\,dx}\, dE \qquad (eq.2)$$

where χ (%) is the enrichment level of the target, N_A (atom·mol^{-1}) is the Avogadro number, λ (s^{-1}) is the decay constant of Tb radionuclides, Z is the charged state of the accelerated ion, e is the elementary charge, A (g.mol^{-1}) is the molar mass of the target nuclei, E_0 (MeV) is the incident beam energy impinging the target, E_1 (MeV) is the beam energy after crossing the target (MeV), E_1 is zero while the charged particles is stopped in the target; σ *(E)* (cm^2) is the cross-section at energy E, and $\frac{dE}{dx}$ (MeV·cm^{-1}) is the linear energy transfer. The unit of the production yield is MBq/µAh.

In this work, the Radionuclide Yield Calculator (RYC) program was used to estimate the production yield (Sitarz, 2019). It is a free GUI program developed by GIP ARRONAX. It uses

SRIM module to calculate the stopping power of the projectiles and calculates the production yield and activity of radioisotopes based on irradiation parameters and excitation functions.

Preparation for thick target irradiation

The enriched thick ${}^{*}Gd_2O_3$ target was encapsulated in a stainless-steel capsule. A Ti foil (supplied by Goodfellow, 99.95% purity) with a thickness of 10 µm was put before the enriched pellet in order to get a measurement of the incident beam intensity through the monitor reactions ${}^{nat}Ti(d,x){}^{48}V$ and ${}^{nat}Ti(d,x){}^{46}Sc$. The schematic diagram of the assembly (a) and the photo of the target and the capsule (b) are shown in Fig. 4.

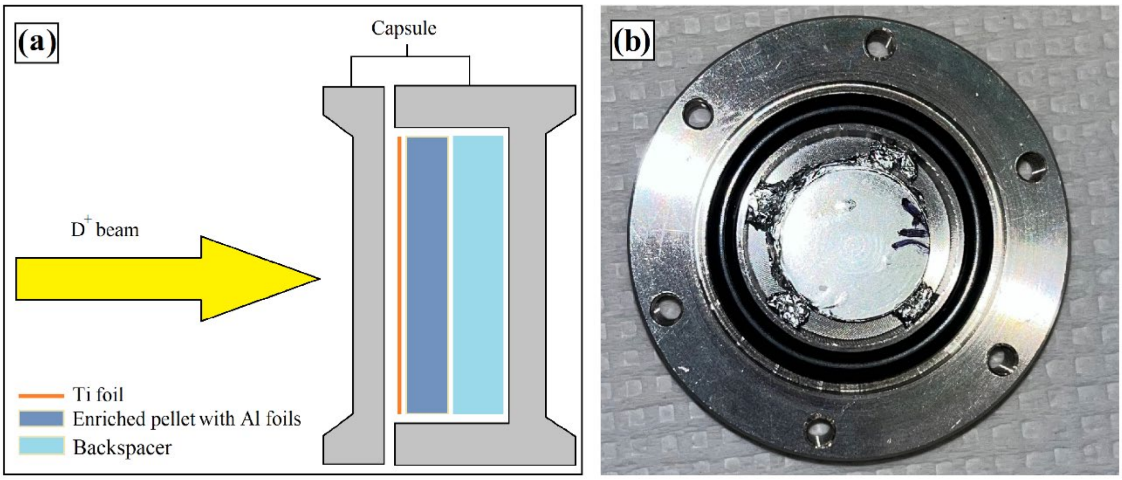

Fig. 4 (a) Schematic diagram of the assembly of Ti foil and pellets in the capsule. The size and thickness of the foils are not drawn according to the real size. (b) Photo of the stack (without the Ti foil) and a part of the capsule.

The assembly was irradiated by deuterons for 1 hour: the incident energy hitting the enriched target was (15.1 ± 1.5) MeV, the exit energy was (8.6 ± 0.2) MeV, and the beam intensity was (368 ± 26) nA.

After irradiation, the whole assembly was stored in a lead pot during 9 days for decay. Then the enriched pellet and aluminum wrapping foils were dissolved in 100 mL of HCl with a concentration of 2 mol/L. The dissolved solution was diluted by a factor 100. Three aliquots were collected for measurements. The data acquisition was performed 9 to 14 days after EOB depending on the aliquot. Each counting was made in contact with the detector and lasted 24 hours. Dead times were 10%, 9%, and 6%, respectively. Reported activities of measured radionuclides correspond to the average values of the three counts.

3. Results and discussion

Cross-section measurements

In this study, the radionuclide of interest is ${}^{155}Tb$ and it was presented in all irradiated targets. Meanwhile, certain radionuclides, which were considered as impurities, such like ${}^{153}Tb$, ${}^{154g}Tb$, ${}^{154m1}Tb$, ${}^{154m2}Tb$, and ${}^{156g}Tb$, were also measured in several targets. The obtained cross-section values and associated uncertainties are listed in Table 4. Data from the TENDL-2021 data library ("TENDL-2021 nuclear data library," n.d.) was used to compare with the measured results, the composition of each Gd isotope in the target was taken into account. Comparisons on ^{153}Tb, ^{154}Tb (including ^{154g}Tb, ^{154m1}Tb and ^{154m2}Tb), ^{155}Tb, and ^{156g}Tb are respectively shown in Fig. 5, Fig. 6, Fig. 7, and Fig. 8.

Table 4 Cross-sections of the reaction *Gd(d,x)Tb

Energy (MeV)	σ ^{153}Tb (mb)	σ ^{154m2}Tb (mb)	σ ^{154m1}Tb (mb)	σ ^{154g}Tb (mb)	σ ^{155}Tb (mb)	σ ^{156g}Tb (mb)
8.1 ± 0.4	-	-	-	-	72.8 ± 9.2	23.1 ± 2.7
9.0 ± 0.4	-	-	-	-	170.3 ± 18.6	41.6 ± 4.5
11.2 ± 0.4	-	-	-	-	256.5 ± 24.9	53.0 ± 5.2
12.4 ± 0.3	-	-	-	-	471.3 ± 48.2	57.3 ± 5.9
14.0 ± 0.4	-	< 5.1	< 19.2	< 5.0	720.8 ± 67.4	78.2 ± 7.4
14.2 ± 0.3	-	< 5.1	< 19.2	< 5.0	797.9 ± 77.8	83.1 ± 8.1
16.0 ± 0.3	-	< 5.1	< 19.2	< 5.0	709.0 ± 66.3	71.4 ± 6.7
19.4 ± 0.3	-	31.6 ± 3.5	104.5 ± 14.8	188.0 ± 26.6	501.0 ± 49.9	62.8 ± 6.2
24.4 ± 0.4	98.3 ± 12.7	43.8 ± 6.3	79.9 ± 11.5	51.3 ± 7.4	343.4 ± 46.7	56.4 ± 6.1
29.7 ± 0.3	837.6 ± 78.8	76.6 ± 9.8	116.9 ± 17.0	134.4 ± 19.5	180.6 ± 24.0	37.2 ± 4.1

^{153}Tb:

The ^{153}Tb ($T_{1/2}$ = 2.34 d) was only detected in two targets at high energies (24.4 MeV and 29.7 MeV). This is expected as the threshold energy of *Gd(d,x)^{153}Tb is 20.17 MeV (Table 3). Fig. 5 shows the comparison between our measured values (black points) and the TENDL-2021 calculation (black curve). The global trend of TENDL-2021 calculation is in general consistent with that of our measurements. At 29.7 MeV, the measured cross-section is 837.6 mb, which is in agreement with the value of TENDL-2021 (875.4 mb) considering the associated uncertainties of the measured value. At 24.4 MeV, our measured value (98.3 mb) is smaller than that of TENDL-2021. Additional data points above 20 MeV are necessary to determine precisely the position and amplitude of the maximum of the cross-section.

^{154g}Tb, ^{154m1}Tb and ^{154m2}Tb:

The ^{154}Tb have three longer lived (half-life longer than 9h) states: a ground state ^{154g}Tb and two metastable states, ^{154m1}Tb and ^{154m2}Tb. The ^{154m2}Tb decays to ^{154}Gd (ε = 98.2%) and ^{154m1}Tb (IT = 1.8%), meanwhile, the ^{154m1}Tb decays to ^{154}Gd (ε = 78.2%) as well as the ground state ^{154g}Tb (IT = 21.8%), and ^{154g}Tb decays with almost 100% ε to ^{154}Gd and less than 0.1% β^{-} to ^{154}Dy (Vermeulen et al., 2012; Tárkányi et al., 2014; Formento-Cavaier et al., 2020). The Bateman equations were used to estimate the cross-section of these three states. As the threshold energies for *Gd(d,x) ^{154g,154m1,154m2}Tb are 13.16 MeV, 13.27 MeV and 13.57 MeV respectively, ^{154g,154m1,154m2}Tb can theoretically be produced when the incident energy is larger than 13.57 MeV. However, according to Table 4, the three states were detected only in three targets at high incident energy (above 19.4 MeV). The cross-sections of ^{154m2}Tb, ^{154m1}Tb, and ^{154g}Tb are maximum at 24.4 MeV, the values are 76.6 mb, 116.9 mb, and 134.4 mb, respectively. The TENDL-2021 calculation was compared with the measured results (Fig. 6). The calculations are represented by curves while the measurements are represented by points. As it can be seen in the figure, the measured cross-sections for ^{154m2}Tb and ^{154g}Tb are much smaller than those provided by TENDL-2021 calculations, while for ^{154m1}Tb, the TENDL-2021 values agree with our higher energy data points. In all this case, also, additional dedicated experiments will be needed to acquire more data points.

^{155}Tb:

The cross-section of the reaction *Gd(d,x)^{155}Tb weas successfully measured in all targets. Values and associated relative uncertainty are listed in Table 4. It can be seen from the table that the cross-section increases from 8.1 MeV to 14.2 MeV where it reaches the highest value of 797.9 mb, then as the energy continues to increase, the cross-section decreases. The uncertainties are between 9% and 14%, the highest relative uncertainty values are for targets having the lowest Gd content (Table 2) which is somewhat expected.
When the incident energy impinging the target is smaller than 12.52 MeV, the only reaction that can produce ^{155}Tb is ^{155}Gd(d,2n)^{155}Tb. Knowing the ^{155}Gd proportion in the enriched target which is 92.8%, the cross-section of this reaction for a target containing 100% ^{155}Gd can therefore be deduced. The results are shown in Table 5. These values are the first experimental cross-section values for this reaction.

Table 5 Cross-section of the reaction ^{155}Gd(d,2n)^{155}Tb converted from measured values of *Gd(n,x)^{155}Tb.

Energy (MeV)	σ ^{155}Tb (mb)
8.1 ± 0.4	78.4 ± 9.9
9.0 ± 0.4	183.5 ± 20.0
11.2 ± 0.4	276.4 ± 26.8
12.4 ± 0.3	507.9 ± 51.9

Table 4 and Table 5 present cross-section data based on a reference half-life of Nudat 3.0. However, recent work by Collins et al. (Collins et al., 2022) updated the half-life of ^{155}Tb to 5.2346(36) d, which differs from the NuDat 3.0 value of 5.32 d. To compare the impact of this update, we compare the measured cross-section data using both half-life values in Fig. 7. As can be observed, the updated half-life leads to a slight decrease in cross-section values. Additionally, the comparison between our measurements and the TENDL-2021 calculations is also presented in the same figure. Overall, the measured results are consistent with TENDL-2021 calculations. However, TENDL-2021 values tend to overestimate the cross-sections when energy is between 10 MeV and 16 MeV, particularly at 11.2 MeV, where the calculated value is nearly twice the measured value. The same overestimation can also be observed in Fig. 8. Meanwhile, above 16.0 MeV, the measurements and the values from the database are in good agreement.

^{156g}Tb:

The radionuclide ^{156}Tb also has a ground state ^{156g}Tb ($T_{1/2}$ = 5.35 d) and two longer-lived metastable states, ^{156m1}Tb ($T_{1/2}$ = 24.4 h) and ^{156m2}Tb ($T_{1/2}$ = 5.3 h). The ^{156m2}Tb decays with almost 100% to the ^{156m1}Tb, and the ^{156m1}Tb decays 100% to the ground state ^{156g}Tb. The gamma energies of the two metastable states are low (E_γ = 49.630 keV for ^{156m1}Tb and E_γ = 88.4 keV for ^{156m2}Tb), making them difficult to measure.Therefore, only the ground state was measured in this work. Since all targets were measured at least 20 h after the EOB, the increase of ^{156g}Tb activity due to decay of metastable states small (Dellepiane et al., 2022). The ^{156g}Tb was detected in all target, this is consistent with value of the threshold energy to produce ^{156g}Tb (Table 3). The cross-section increases with the incident energy and reaches to the maximum value of 85 mb at 15 MeV, then it decreases as energy continues to increase. TENDL-2021 calculation is in overall agreement with our measured values, except for values at around 11.2 MeV and 12.4 MeV, the calculation overestimates the cross-sections (Fig. 8).

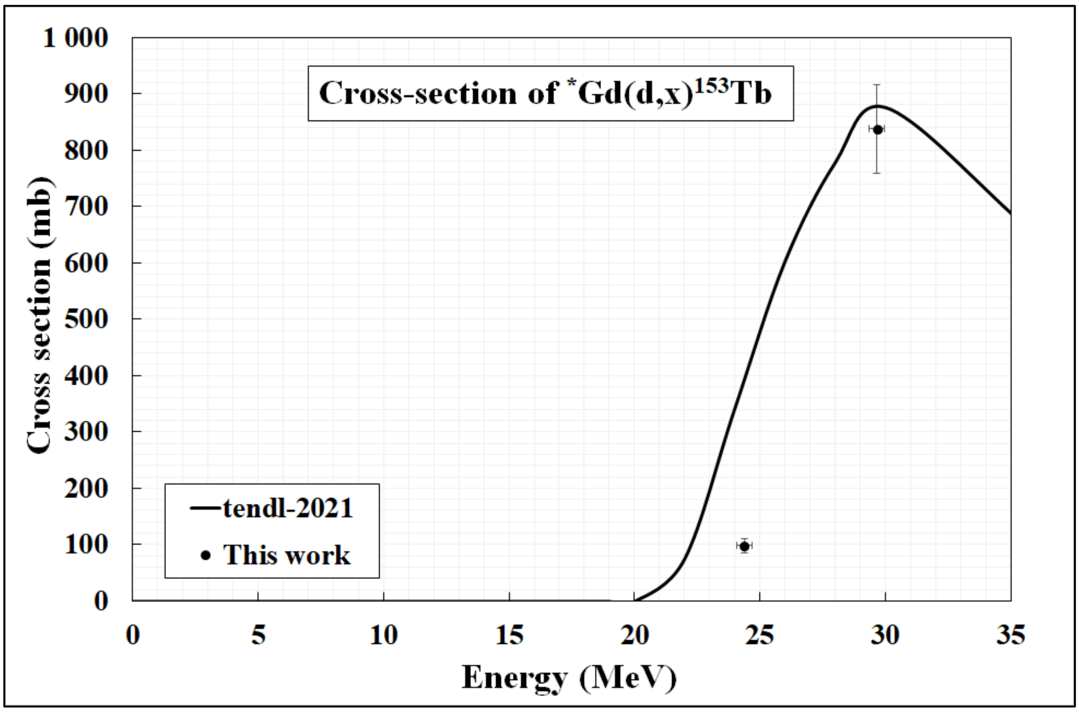

Fig. 5 Comparison of measured cross-section (black points) and TENDL-2021 values (black curve) of the reaction *Gd(d,x)^{153}Tb.

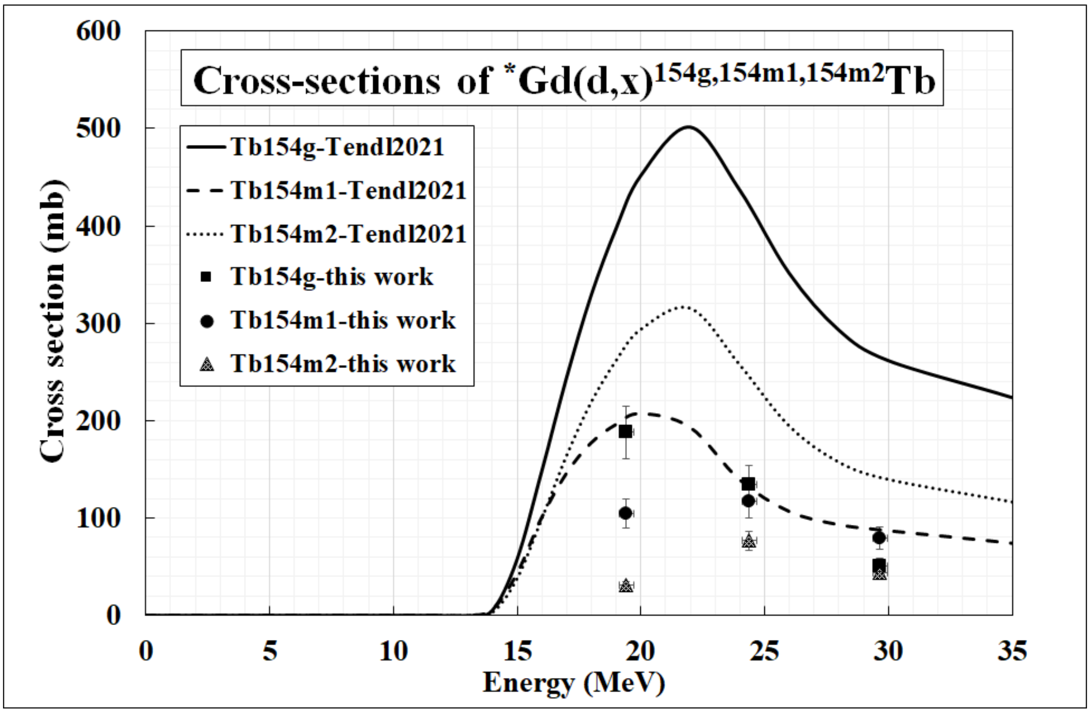

Fig. 6 Comparison of measured cross-sections and simulated values of the reaction *Gd(d,x)^{154g,154m1,154m2}Tb. The curves represent TENDL-2021 values and the points represent the measured values.

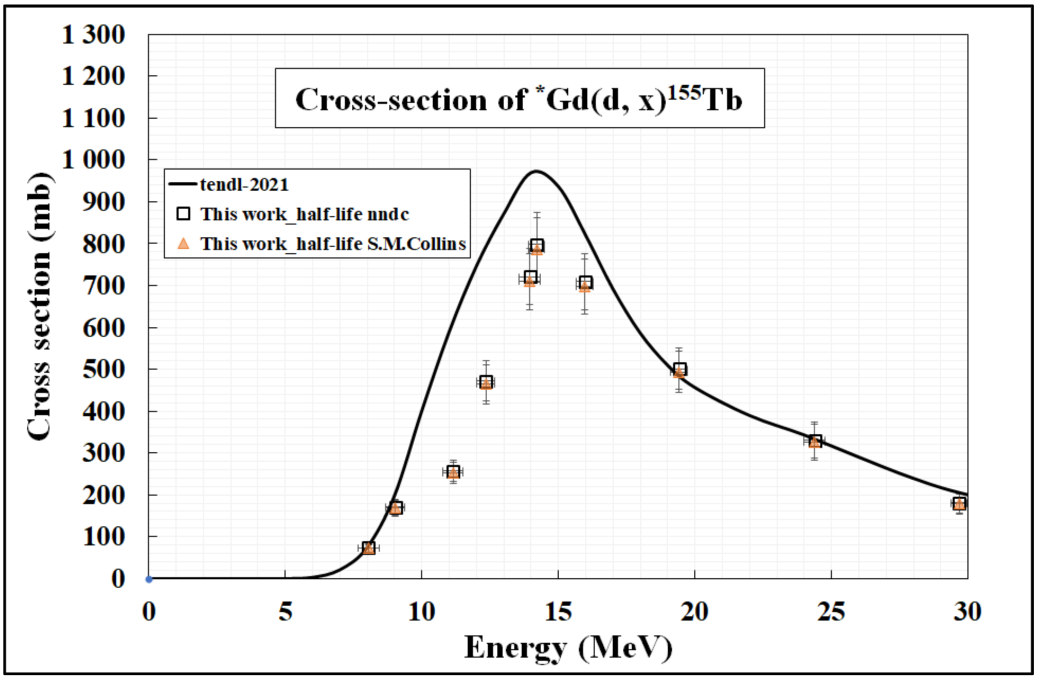

Fig. 7 Comparison of measured cross-section (square or triangle symbols) and TENDL-2021 calculations (black curve) of the reaction *Gd(d,x)^{155}Tb. Black square symbols present cross-section values use half-life of NuDat 3.0 while orange triangle symbols use half-life measured by Collins et al..

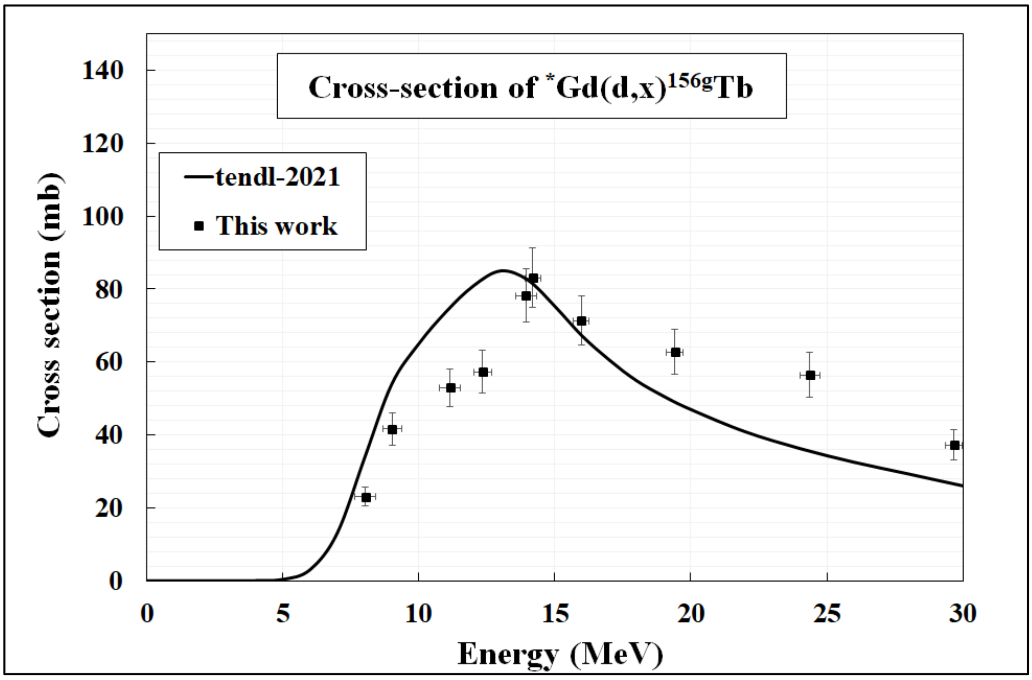

Fig. 8 Comparison of measured cross-section (black points) and TENDL-2021 calculations (black curve) of the reaction *Gd(d,x)^{156g}Tb.

Production yield and purity estimation

Using our measured cross-sections, fitted excitation functions can be estimated using the Experimentally Modified Gaussian (EMG) distribution model. In this work, except for the radionuclide of interest, ^{155}Tb, the production yield of ^{156g}Tb has also been investigated since it is the only impurity that cannot be removed by decay or chemical separation. The fitted excitation functions of *Gd(d,2n)^{155}Tb and *Gd(d,n)^{156g}Tb are respectively shown in Fig. 9 (A) and (B).

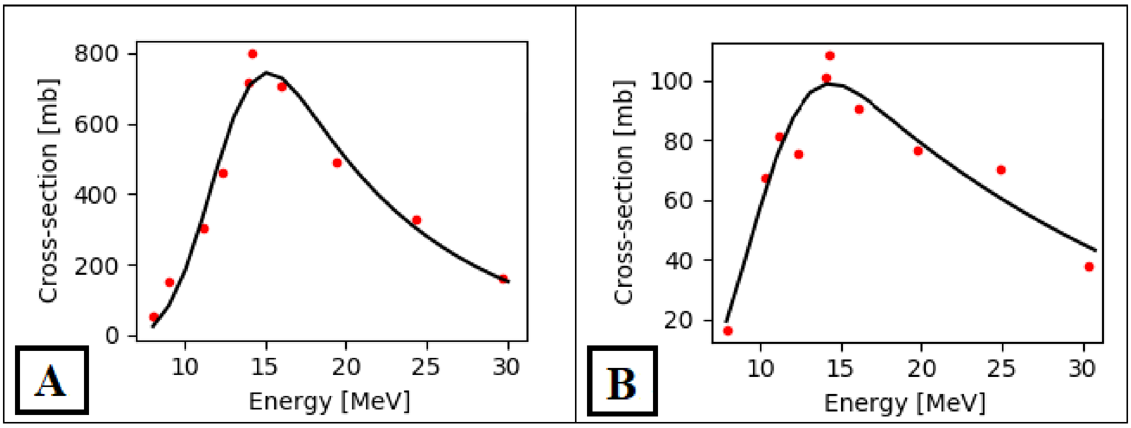

Fig. 9 Fitted excitation function of ^{155}Tb (A) and ^{156g}Tb (B) using the Experimentally Modified Gaussian (EMG) distribution model.

From these fitted excitation functions, the production yields have been estimated using *eq.2*. Fig. 10 shows the RYC estimation of the production yield, the continuous line and the dashed line represent respectively the production yield of ^{155}Tb and ^{156g}Tb using our measured data. It should be noted that the value plotted for a given energy in the figure is determined assuming that the target thickness is large enough to stop the beam in it. For ^{155}Tb, the production yield increased slowly when the incident energy increase from 8 to 13 MeV, then, the production yield increases rapidly as the energy continues to increase at 13-19 MeV and finally slow down at 19-30 MeV. From this curve, it is possible to determine the value for any energy interval (incident energy E_0, output energy E_1) by just making the difference between the yields corresponding to E_0 and E_1.

From the RYC simulation of production yields, the ratio of the production yield of ^{155}Tb to the production yield of ^{156g}Tb can thus be estimated for our target material *Gd (Fig. 11). The ratio increases from 60% to 89% when energy increases from 9 MeV to 18 MeV, and remains unchanged from 18 MeV to 22 MeV, then the ratio slightly decreases to 87% when energy increases to 30 MeV. This ratio helps to estimate the purity of ^{155}Tb after the decay of ^{153}Tb or ^{154}Tb (in general several days after the EOB) as ^{156g}Tb and ^{155}Tb have similar half-lives and decay will not affect it. Going to higher enrichment of the target material will help increase the purity. However, with deuteron beam, even in the case of a 100% enrichment, there will be ^{156g}Tb produced limiting the final purity to 95%.

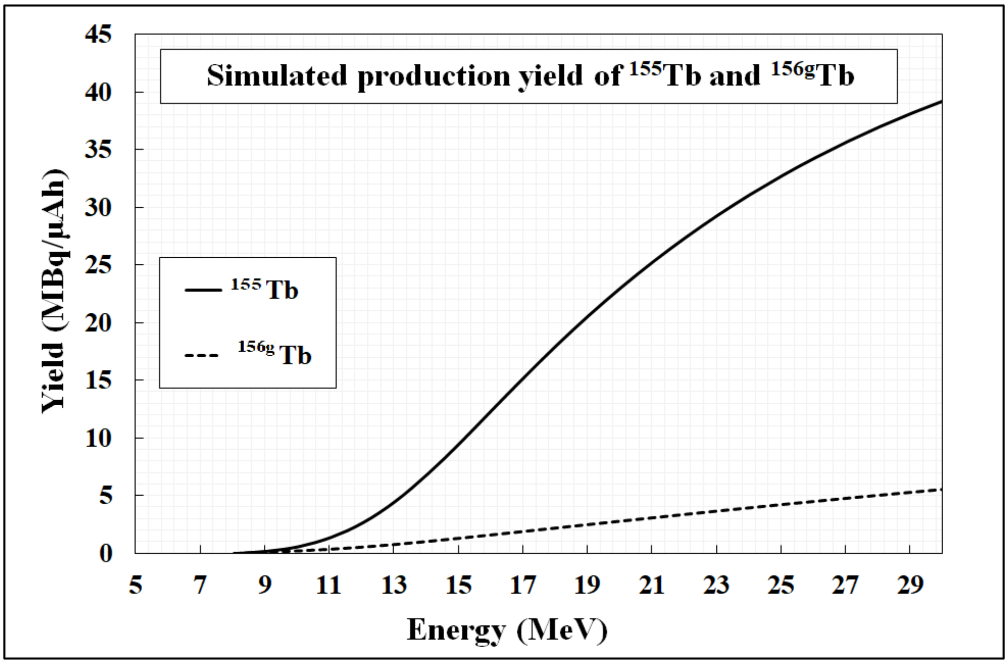

Fig. 10 RYC simulation of production yield of ^{155}Tb (continuous line) and ^{156g}Tb (dashed line) using measured data.

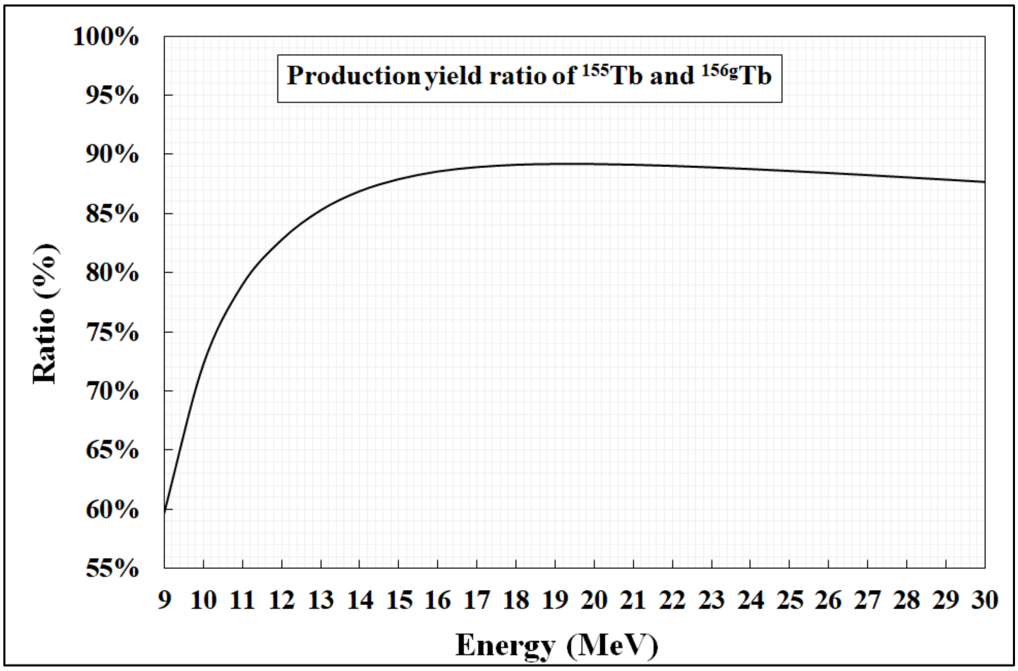

Fig. 11 The ratio of the production yield of ^{155}Tb and ^{156g}Tb as a function of energy using the data simulated by RYC.

Thick target production

When the incident energy hitting the enriched target was (15.1 ± 1.5) MeV and the exit energy was (8.6 ± 0.2) MeV, experimental production yields of the enriched $^{*}Gd_2O_3$ target at EOB were estimated to be 10.2 ± 0.7 MBq/µAh for ^{155}Tb and 1.3 ± 0.1 MBq/µAh for ^{156g}Tb. These experimental production yields show a very good agreement with the one calculated from our cross-section data using RYC which are 10.1 MBq/µAh and 1.2 MBq/µAh for ^{155}Tb and ^{156g}Tb respectively. This agreement shows a great consistency between all our experiments.

The purity of ^{155}Tb, which is defined in this work to be the ratio of the activity of ^{155}Tb to the total activity of all radionuclides (^{154m1,m2,g}Tb, ^{155}Tb and ^{156g}Tb), was estimated according to the first counting and using the decay equations. The change of purity over time is shown in Fig. 12. It is clear that the purity increases with cooling time (decay of ^{153}Tb and ^{154}Tb) but in low proportion: from 9 days after EOB to 14 days after EOB, the purity increases from 87.6% to 88.6%. The purity remains almost unchanged after 14 days. The final production yield for ^{155}Tb is (3.2 ± 0.2) MBq/µAh after 9 days of decay and (1.6 ± 0.2) MBq/µAh after 14 days of decay.

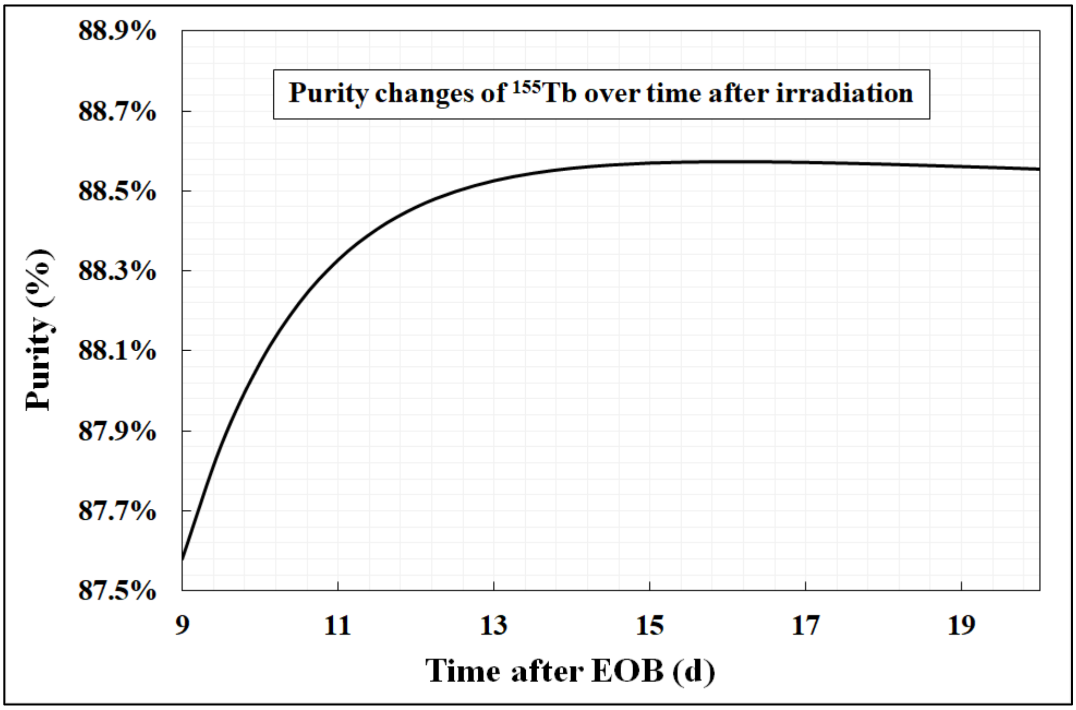

Fig. 12 Purity changes of ^{155}Tb as a function of time after irradiation. The purity here is defined as the ratio of activity of ^{155}Tb and other radionuclides (^{154m1,m2,g}Tb, ^{155}Tb and ^{156g}Tb), it is estimated by decay equations.

The experimental production yield of ^{155}Tb has also been compared with proton-induced production route ^{155}Gd(p,n)^{155}Tb (Dellepiane et al., 2022). The comparison is presented in Table 6. It can be seen that, under the respective optimum experimental conditions, the production yield of deuteron-induced reaction (this work) is nearly three times higher than that of proton-induced reaction. However, the purity obtained with deuteron is smaller than that obtained in the proton production route. The latter being able to benefit more from an increase of the ^{155}Gd enrichment.

Table 6 Comparison of different production routes of ^{155}Tb

Production route	Target mass (mg)	Beam incident energy (MeV)	Production yield EOB (MBq/µAh)	Maximum purity (%)
^{155}Gd(d,2n)^{155}Tb	630	15.1	10.2 ± 0.7	89%
^{155}Gd(p,n)^{155}Tb	37-40	10.4	3.4 ± 0.5	93%

4. Conclusion and perspectives

In this work, we explore the potential of an alternative method to produce Tb radionuclide with light-charged-particle-induced reaction on enriched Gd target. The production of ^{155}Tb using deuteron beam was taken as a case study.

Using 10 enriched thin Gd targets, the cross-section of the reaction ^{155}Gd(d,2n)^{155}Tb was measured at GIP ARRONAX cyclotron facility at low energy (8-30 MeV) as well as those of other terbium isotopes that will have a direct impact on the purity of the final product. A particular attention has been devoted to ^{153}Tb, ^{154}Tb and ^{156g}Tb. The first two impurities have a relative shorter half-life as compared to ^{155}Tb, and their amount can be reduced by allowing decay. However, the latter, ^{156g}Tb, has a half-life similar to ^{155}Tb and is produced on the same energy range as ^{155}Tb, it will remain the main contaminant to deal with. From our cross-section measurement values, the production yield and the ratio between ^{155}Tb and ^{156g}Tb were estimated allowing to characterize the purity of the final product.

For thick target production, one enriched $^{*}Gd_2O_3$ target was irradiated by deuteron beam with a beam intensity of 368 nA for 1 h. The thick production yields of ^{155}Tb and ^{156g}Tb were experimentally measure to be respectively 10.2 MBq/µAh and 1.3 MBq/µAh at EOB. After 14 days of decay, the purity of ^{155}Tb was measured to be 89%. These results are in agreement with calculated value obtained starting from experimental cross-sections values and using RYC calculations. This thick target experiment shows the good consistency of our work and the reliability of our cross-section experiments. Compared to proton-induced reaction, the production yield with deuteron is three times higher, but the final purity of ^{155}Tb is lower.

In summary, this work exemplifies the interest of light charged particle irradiation of enriched gadolinium target to produce efficiently terbium radionuclides. Deuteron-induced reaction on Gd target can be a route for Tb production as it is often more productive than the proton one. However, purity of the final product must be looked carefully. Better purity will require higher enrichment level of gadolinium isotopes. Improvement of mass separation can also help if yields are improved.

Only one low intensity thick target production test was carried out in this work and it will be interesting to investigate further high intensity production yield of terbium from enriched gadolinium target by working on enriched metallic gadolinium targets and on dedicated targetry systems to allow high intensity irradiations.

Acknowledgment

The cyclotron Arronax is supported by CNRS, Inserm, INCa, the Nantes University, the Regional Council of Pays de la Loire, local authorities, the French government and the European Union. This work has been, in part, supported by grants from the French National Agency for Research called "France 2030 investment plan", Equipex ArronaxPlus (ANR-11-EQPX-0004), Labex IRON (ANR-11-LABX-0018) and ISITE NExT (ANR-16-IDEX-0007). It has also been supported partly through funding from the European Union’s Horizon 2020 research and innovation program under grant agreement No 101008571 (PRISMAP).

References

Alcocer-Ávila, M.E., Ferreira, A., Quinto, M.A., Morgat, C., Hindié, E., Champion, C., 2020. Radiation doses from 161Tb and 177Lu in single tumour cells and micrometastases. EJNMMI Phys 7, 33. https://doi.org/10.1186/s40658-020-00301-2

Allen, B.J., Goozee, G., Sarkar, S., Beyer, G., Morel, C., Byrne, A.P., 2001. Production of terbium-152 by heavy ion reactions and proton induced spallation. Applied Radiation and Isotopes 54, 53–58. https://doi.org/10.1016/S0969-8043(00)00164-0

Baum, R.P., Singh, A., Kulkarni, H.R., Bernhardt, P., Rydén, T., Schuchardt, C., Gracheva, N., Grundler, P.V., Köster, U., Müller, D., 2021. First-in-humans application of 161Tb: A feasibility study using 161Tb-DOTATOC. Journal of Nuclear Medicine 62, 1391–1397. https://doi.org/10.2967/jnumed.120.258376

Beyer, G.-J., Miederer, M., Vranješ-Đurić, S., Čomor, J.J., Künzi, G., Hartley, O., Senekowitsch-Schmidtke, R., Soloviev, D., Buchegger, F., and the ISOLDE Collaboration, 2004. Targeted alpha therapy in vivo: direct evidence for single cancer cell kill using 149Tb-rituximab. Eur J Nucl Med Mol Imaging 31, 547–554. https://doi.org/10.1007/s00259-003-1413-9

Collins, S.M., Robinson, A.P., Ivanov, P., Köster, U., Cocolios, T.E., Russell, B., Webster, B., Fenwick, A.J., Duchemin, C., Ramos, J.P., Chevallay, E., Jakobsson, U., Stegemann, S., Regan, P.H., Stora, T., 2022. Half-life determination of 155Tb from mass-separated samples produced at CERN-MEDICIS. Applied Radiation and Isotopes 190, 110480. https://doi.org/10.1016/j.apradiso.2022.110480

Decay data search [WWW Document], n.d. URL http://nucleardata.nuclear.lu.se/toi/ (accessed 3.30.22).

Dellepiane, G., Casolaro, P., Favaretto, C., Grundler, P., Mateu, I., Scampoli, P., Talip, Z., van der Meulen, N.P., Braccini, S., 2022. Cross-section measurement of terbium radioisotopes for an optimized 155Tb production with an 18 MeV medical PET cyclotron. Applied Radiation and Isotopes 110175. https://doi.org/10.1016/j.apradiso.2022.110175

Duchemin, C., Guertin, A., Haddad, F., Michel, N., Métivier, V., 2016. Deuteron induced Tb-155 production, a theranostic isotope for SPECT imaging and auger therapy. Applied Radiation and Isotopes 118, 281–289. https://doi.org/10.1016/j.apradiso.2016.09.030

Duchemin, C., Ramos, J.P., Stora, T., Aubert, E., Audouin, N., Barbero, E., Barozier, V., Bernardes, A.P., BERTREIX, P., Boscher, A., BURNEL, D., Catherall, R., Cirilli, M., Chevalley, E., Cocolios, T.E., Comte, J., Crepieux, B., Deschamps, M., Dockx, K., Dorsival, A., Fedosseev, V.N., Fernier, P., Formento-Cavaier, R., Gadelshin, V.M., Gilardoni, S., Grenard, J.L., Haddad, F., Heinke, R., juif, b., Khan, M., Köster, U., Lambert, L., lilli, g., lunghi, g., Marsh, B.A., Martinez Palenzuela, Y., Martins, R., Marzari, S., Menaa, N., Michel, N., Pozzi, F., Riccardi, F., riegert, j., riggaz, n., Rothe, S., Stegemann, S., Talip, Z., thiboud, j., van der meulen, n. p., Vollaire, J., vuong, n. t., Wendt, K., Wilkins, S., 2020. CERN-MEDICIS: A UNIQUE FACILITY FOR THE PRODUCTION OF NONCONVENTIONAL RADIONUCLIDES FOR THE MEDICAL RESEARCH, in: 11th International Particle Accelerator Conference. Caen, France. https://doi.org/10.18429/JACoW-IPAC2020-THVIR13

Formento-Cavaier, R., Haddad, F., Alliot, C., Sounalet, T., Zahi, I., 2020. New excitation functions for proton induced reactions on natural gadolinium up to 70 MeV with focus on 149Tb production. Nuclear Instruments and Methods in Physics Research Section B: Beam Interactions with Materials and Atoms 478, 174–181. https://doi.org/10.1016/j.nimb.2020.06.029

Gracheva, N., Müller, C., Talip, Z., Heinitz, S., Köster, U., Zeevaart, J.R., Vögele, A., Schibli, R., van der Meulen, N.P., 2019. Production and characterization of no-carrier-added 161Tb as an alternative to the clinically-applied 177Lu for radionuclide therapy. EJNMMI Radiopharmacy and Chemistry 4, 12. https://doi.org/10.1186/s41181-019-0063-6

Güray, R.T., Özkan, N., Yalçın, C., Rauscher, T., Gyürky, G., Farkas, J., Fülöp, Z., Halász, Z., Somorjai, E., 2015. Measurements of Gd 152 (p, γ) Tb 153 and Gd 152 (p, n) Tb 152 reaction cross sections for the astrophysical γ process. Physical Review C 91, 055809. https://doi.org/10.1103/PhysRevC.91.055809

Hermanne, A., Takacs, S., Adam-Rebeles, R., Tárkányi, F., Takács, M.P., 2013. New measurements and evaluation of database for deuteron induced reaction on Ni up to 50 MeV. Nuclear Instruments and Methods in Physics Research Section B: Beam Interactions with Materials and Atoms 299, 8–23. https://doi.org/10.1016/j.nimb.2013.01.005

Herzog, H., Rösch, F., Stöcklin, G., Lueders, C., Qaim, S.M., Feinendegen, L.E., 1993. Measurement of pharmacokinetics of yttrium-86 radiopharmaceuticals with PET and radiation dose calculation of analogous yttrium-90 radiotherapeutics. J Nucl Med 34, 2222–2226.

Lahiri, S., Nayak, D., Das, S.K., Ramaswami, A., Manohor, S.B., Das, N.R., 1999. Separation of carrier free152, 153Dy and151–153Tb from16O7+ irradiated CeO2 by liquid-liquid extraction. Journal of radioanalytical and nuclear chemistry 241, 201–206. https://doi.org/10.1007/BF02347313

Maiti, M., 2011. New measurement of cross sections of evaporation residues from the nat Pr+ 12 C reaction: A comparative study on the production of 149 Tb. Physical Review C 84, 044615. https://doi.org/10.1103/PhysRevC.84.044615

Müller, C., Fischer, E., Behe, M., Köster, U., Dorrer, H., Reber, J., Haller, S., Cohrs, S., Blanc, A., Grünberg, J., Bunka, M., Zhernosekov, K., van der Meulen, N., Johnston, K., Türler, A., Schibli, R., 2014. Future prospects for SPECT imaging using the radiolanthanide terbium-155 — production and preclinical evaluation in tumor-bearing mice. Nuclear Medicine and Biology 41, e58–e65. https://doi.org/10.1016/j.nucmedbio.2013.11.002

Müller, C., Zhernosekov, K., Köster, U., Johnston, K., Dorrer, H., Hohn, A., Walt, N.T. van der, Türler, A., Schibli, R., 2012. A Unique Matched Quadruplet of Terbium Radioisotopes for PET and SPECT and for α- and β−-Radionuclide Therapy: An In Vivo Proof-of-Concept Study with a New Receptor-Targeted Folate Derivative. Journal of Nuclear Medicine 53, 1951–1959. https://doi.org/10.2967/jnumed.112.107540

Nayak, D., Lahiri, S., Ramaswami, A., Manohar, S.B., Das, N.R., 1999. Separation of carrier free 151,152 Tb produced in 16O irradiated lanthanum oxide matrix. Applied radiation and isotopes 51, 631–636. https://doi.org/10.1016/S0969-8043(99)00106-2

Nigron, E., Guertin, A., Haddad, F., Sounalet, T., 2021. Is 70Zn(d,x)67Cu the Best Way to Produce 67Cu for Medical Applications? Frontiers in Medicine 8. https://doi.org/10.3389/fmed.2021.674617

NuDat 3.0 [WWW Document], n.d. URL https://www.nndc.bnl.gov/nudat3/ (accessed 3.22.22).

Qaim, S.M., Scholten, B., Neumaier, B., 2018. New developments in the production of theranostic pairs of radionuclides. J Radioanal Nucl Chem 318, 1493–1509. https://doi.org/10.1007/s10967-018-6238-x

Q-value Calculator (QCalc) [WWW Document], n.d. URL https://www.nndc.bnl.gov/qcalc/ (accessed 5.31.22).

Sitarz, M., 2019. Research on production of new medical radioisotopes with cyclotron [D]. warsaw university; université de Nantes, 2019. https://theses.hal.science/tel-02458431.

Steyn, G.F., Vermeulen, C., Szelecsényi, F., Kovács, Z., Hohn, A., van der Meulen, N.P., Schibli, R., van der Walt, T.N., 2014. Cross sections of proton-induced reactions on 152Gd, 155Gd and 159Tb with emphasis on the production of selected Tb radionuclides. Nuclear Instruments and Methods in Physics Research Section B: Beam Interactions with Materials and Atoms 319, 128–140. https://doi.org/10.1016/j.nimb.2013.11.013

Szelecsényi, F., Kovács, Z., Nagatsu, K., Zhang, M.-R., Suzuki, K., 2016. Investigation of deuteron-induced reactions on natGd up to 30 MeV: possibility of production of medically relevant 155Tb and 161Tb radioisotopes. J Radioanal Nucl Chem 307, 1877–1881. https://doi.org/10.1007/s10967-015-4528-0

Tárkányi, F., Hermanne, A., Takács, S., Ditrói, F., Csikai, J., Ignatyuk, A.V., 2013. Cross-section measurement of some deuteron induced reactions on 160Gd for possible production of the therapeutic radionuclide 161Tb. J Radioanal Nucl Chem 298, 1385–1392. https://doi.org/10.1007/s10967-013-2507-x

Tárkányi, F., Takács, S., Ditrói, F., Csikai, J., Hermanne, A., Ignatyuk, A.V., 2014. Activation cross-sections of deuteron induced reactions on natGd up to 50MeV. Applied Radiation and Isotopes 83, 25–35. https://doi.org/10.1016/j.apradiso.2013.10.010

TENDL-2021 nuclear data library [WWW Document], n.d. URL https://tendl.web.psi.ch/tendl_2021/tendl2021.html (accessed 3.13.23).

Vermeulen, C., Steyn, G.F., Szelecsényi, F., Kovács, Z., Suzuki, K., Nagatsu, K., Fukumura, T., Hohn, A., van der Walt, T.N., 2012. Cross sections of proton-induced reactions on natGd with special emphasis on the production possibilities of 152Tb and 155Tb. Nuclear Instruments and Methods in Physics Research Section B: Beam Interactions with Materials and Atoms 275, 24–32. https://doi.org/10.1016/j.nimb.2011.12.064

Wang, Y., Sounalet, T., Guertin, A., Haddad, F., Michel, N., Nigron, E., 2022. Electrochemical co-deposition of Ni–Gd2O3 for composite thin targets preparation: Production of 155Tb as a case study. Applied Radiation and Isotopes 110287. https://doi.org/10.1016/j.apradiso.2022.110287

Yordanova, A., Eppard, E., Kürpig, S., Bundschuh, R.A., Schönberger, S., Gonzalez-Carmona, M., Feldmann, G., Ahmadzadehfar, H., Essler, M., 2017. Theranostics in nuclear medicine practice. Onco Targets Ther 10, 4821–4828. https://doi.org/10.2147/OTT.S140671

Ziegler, J.F., Ziegler, M.D., Biersack, J.P., 2010. SRIM – The stopping and range of ions in matter (2010). Nuclear Instruments and Methods in Physics Research Section B: Beam Interactions with Materials and Atoms, 19th International Conference on Ion Beam Analysis 268, 1818–1823. https://doi.org/10.1016/j.nimb.2010.02.091

Figure Captions

Fig. 1 The photo of a thin target (target #4) made by co-electrodeposition technique. The thickness is 18 μm and the diameter of the deposit is 1.5 cm.

Fig. 2 Packaging process of the thick ${}^{*}Gd_2O_3$ pellet: (a) the enriched pellet made by the press; (b) the hand wrapped pellet by two aluminum foils; (c) the wrapped pellet in the press die; (d) the tightly wrapped pellet after the compression.

Fig. 3 (a) Schematic diagram of the stack composition used for a typical experiment where two targets were irradiated simultaneously. The size and thickness of the foils are not drawn according to the real scale. (b) Photo of the stack (without the first Ti foil) and the two parts of the capsule.

Fig. 4 (a) Schematic diagram of the assembly of Ti foil and pellets in the capsule. The size and thickness of the foils are not drawn according to the real size. (b) Photo of the stack (without the Ti foil) and a part of the capsule.

Fig. 5 Comparison of measured cross-section (black points) and TENDL-2021 values (black curve) of the reaction ${}^{*}Gd(d,x)^{153}Tb$.

Fig. 6 Comparison of measured cross-sections and simulated values of the reaction ${}^{*}Gd(d,x)^{154g,154m1,154m2}Tb$. The curves represent TENDL-2021 values and the points represent the measured values.

Fig. 7 Comparison of measured cross-section (square or triangle symbols) and TENDL-2021 calculations (black curve) of the reaction ${}^{*}Gd(d,x)^{155}Tb$. Black square symbols present cross-section values use half-life of NuDat 3.0 while orange triangle symbols use half-life measured by Collins et al..

Fig. 8 Comparison of measured cross-section (black points) and TENDL-2021 calculations (black curve) of the reaction ${}^{*}Gd(d,x)^{156g}Tb$.

Fig. 9 Fitted excitation function of ${}^{155}Tb$ (A) and ${}^{156g}Tb$ (B) using the Experimentally Modified Gaussian (EMG) distribution model.

Fig. 10 RYC simulation of production yield of ${}^{155}Tb$ (continuous line) and ${}^{156g}Tb$ (dashed line) using measured data.

Fig. 11 The ratio of the production yield of ${}^{155}Tb$ and ${}^{156g}Tb$ as a function of energy using the data simulated by RYC.

Fig. 12 Purity changes of ${}^{155}Tb$ as a function of time after irradiation. The purity here is defined as the ratio of activity of ${}^{155}Tb$ and other radionuclides (${}^{154m1,154m2,154g}Tb$, ${}^{155}Tb$ and ${}^{156g}Tb$), it is estimated by decay equations.